Journal of Photonics for Energy

PhotonicsforEnergy.SPIEDigitalLibrary.org

Visual appearance of microcontacts for solar windows

Lucas J. Myers
Harry A. Atwater
Rebecca Saive

SPIE.

Lucas J. Myers, Harry A. Atwater, Rebecca Saive, "Visual appearance of microcontacts for solar windows," *J. Photon. Energy* **9**(2), 027001 (2019), doi: 10.1117/1.JPE.9.027001.

Visual appearance of microcontacts for solar windows

Lucas J. Myers,[a] Harry A. Atwater,[b] and Rebecca Saive[a,*]
[a]University of Twente, Complex Photonic Systems, Mesa+ Institute for Nanotechnology, Enschede, The Netherlands
[b]California Institute of Technology, Pasadena, California, United States

Abstract. We explore the visual appearance of microscale silver grids for use in solar windows. The distortion of view is investigated by ray optical computations and experiments. We find that the visual appearance strongly depends on the geometric properties of the microcontacts (i.e., shape, aspect ratio, and periodicity) as well as on the viewing angle. From a perpendicular view, glass substrates appear marginally darker with microcontacts. In the case of effectively transparent triangular cross-section microcontacts, observation of scenes under a steep angle with respect to the substrate leads to the appearance of "ghost images." Scenes are projected through redirection of rays by triangular cross-section microcontacts which can be tuned by adjusting aspect ratio and periodicity. [DOI: 10.1117/1.JPE.9.027001]

Keywords: transparent contacts; building integrated photovoltaics; optical simulations.

Paper 19009 received Feb. 4, 2019; accepted for publication Apr. 17, 2019; published online May 13, 2019.

1 Introduction

Extracting charge carriers efficiently from photovoltaic devices is one of the key challenges the solar industry is facing. In solar cells either metal contact grids and/or transparent conductive oxides (TCOs) provide lateral conduction paths for charge carriers.[1] In general, a trade-off exists between maximizing light absorption and minimizing electric losses, as metal contacts on the front reflect light and TCOs parasitically absorb light. These shading and absorption mechanisms lead to 5% to 10% photon loss and contribute the largest single loss mechanism in commercial solar cells. Recently, we invented a technology that can mitigate these optical losses without diminishing the electrical performance: effectively transparent contacts (ETCs).[2–4] These ETCs are triangular cross-section microscale silver grids that redirect incoming photons efficiently to the active area of the solar cell. In computations and experiments, we demonstrated effective transparency of 99.9% as well as support with light trapping in thin film and bifacial technology.[5,6] The effective transparency T_{eff} is defined as the ratio between the light intensity transmitted through the front contact layer/grid I_T and the incident light intensity I_0 ($T_{\text{eff}} = I_T/I_0$). In the case of ETCs, this transmission is achieved through forward redirection at the specular sidewalls of the ETCs. Therefore, ETCs provide effective transparency through efficient redirection and not through high transmittance.

Extracting charge carriers becomes an even bigger challenge if front and rear contacts need to be transparent, such as is the case for solar windows.[7–9] Solar windows increasingly gain importance in building integrated photovoltaics. Several thin film technologies such as organic[7] and perovskite[10] solar cells have been proposed to act as (semi-) transparent semiconducting absorber layers. In all cases, transparent conductors are necessary on the front and rear sides in order to provide the visual appearance desired for window applications. For large windows, the sheet resistance of TCOs alone is not sufficiently low to provide low loss lateral charge transport.[11] Therefore, metal grids need to be incorporated[11,12] that compromise on the visual appearance and give a "technical" look to the windows, unwanted by many consumers. In addition, these metal grids reflect 4% to 7% of the incoming light and thereby reduce the performance of solar

*Address all correspondence to Rebecca Saive, E-mail: r.saive@utwente.nl

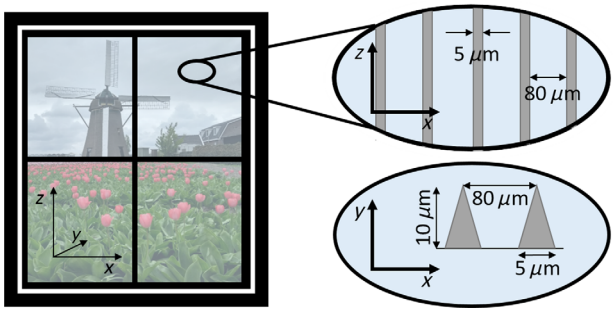

Fig. 1 Schematic of an ETC window: triangular cross-section microsilver grids are integrated with a glass window.

windows. We incorporated ETCs into superstrates[13] for solar cells in order to resolve these issues and boost the power output of thin film solar cells.

From our previous studies, we learned that ETCs transmit almost all of the incident light which leads to a relative solar cell efficiency enhancement of 4% to 10%, depending on the front contact that is replaced.[2–6,13,14] The reason for this high transmission is the redirection of light to the active area of the solar cell. The redirected light enters the solar cell under an altered angle and in a solar window a portion of this light is transmitted. In order to understand how this process affects the visual appearance of windows with ETCs—which we call ETC windows (Fig. 1)—an optical model is needed that takes the properties of the human eye into account. Here, we present such a model, compare our model with experimental results, and present the visual appearance of ETC windows and of windows with flat microcontacts under different viewing conditions and with different geometries. We find that from a perpendicular view, ETC windows and windows with flat microcontacts appear marginally darker than normal windows. Observation of scenes through ETC windows under an angle leads to the appearance of "ghost images," scenes projected through redirection of rays by ETCs, that can be tuned by adjusting the geometry.

2 Computational Model

We performed computational simulations in order to obtain an accurate description of how a human eye perceives scenes observed through ETC windows. The model uses a ray optical approach adjusted to human eye resolution and depth perception as detailed below.

2.1 *Ray Optical Model*

Our ray optical model is a standard emulation of a pinhole camera, optimized by tracing rays in reverse.[15] Physically, in a pinhole camera, rays are incident through a small opening in an otherwise lightproof box, projecting an image on its back wall. This image is a point reflection of the original scene. As the ray trajectories are symmetric about the pinhole, we can avoid the point reflection by instead thinking of rays passing through an image plane outside the box. If we were to project only the rays which pass through the pinhole aperture onto this image plane, we would get an image identical to that on the back wall of the box, only inverted. Thus, since we are only interested in rays which pass through the pinhole, we can generate rays which start there and span a grid on the image plane, with grid-points corresponding to pixels of an image. The pixel values are obtained by finding intersections between rays and other objects in the environment. This method creates an image identical to the one with rays generated from the environment and moving toward the pinhole, but with the advantage of disregarding rays which do not pass through the aperture.[16]

For further optimization, the only objects which were physically modeled were the window and the ETCs. The window was treated as two refractive planes, and the ETCs were modeled as triangular prisms with reflective surfaces. A schematic of this model is presented in Fig. 2. We used 360 deg images to approximate the outside environment. To simulate the experiment,

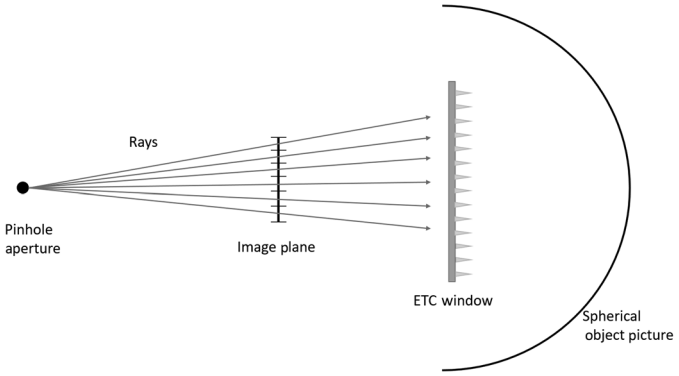

Fig. 2 Schematic of the ray optical model.

the image used was an almost entirely dark sphere with a picture of a tree[17] placed on a small patch in the direction of ray propagation. To simulate an observer looking through the window from a dark room, a 360-deg scene of a beach was used,[18] with the back hemisphere blacked out which corresponds to a dark room without illumination or reflective surfaces. In the simulation, we rotated the window about an axis which ran parallel to the ETCs to investigate the role of viewing angle in the visual appearance.

2.2 *Human Eye Resolution*

In order to accurately capture how the presence of ETCs affects the image, we set the ray density high enough so that adjacent rays would not pass over a contact. With windows at a distance of 25 cm, and contacts with a width of 5 μm, this equates to an angular spacing of 0.00002 rad between rays. This ray density produces a much higher resolution image than the eye, which has an approximate angular resolution of 0.0003 rad.[19] To lower the resolution to that of the eye, we used a bicubic interpolation wherein the output pixel value is a weighted average of pixels in the nearest four-by-four neighborhood. This was done using MATLAB's imresize function.

2.3 *Depth of Field*

While the pinhole model's infinitely small aperture allows for a more efficient program, it creates an artificially clear image when compared to one generated by the eye. Because the eye is a finite aperture-lens system, it must focus at a particular depth, blurring objects which are closer or further than the given focal plane. This occurs because rays emanating from a point source not in the focal plane are not focused to a point on the image plane, rather, they are projected to a region. This region is called the circle of confusion and its diameter can be calculated geometrically.[20]

To capture this effect while still using our pinhole model, we must use a synthetic depth of field algorithm. We chose to use the "Forward-Mapped Z-Buffer" method, wherein pixels are sorted into different planes based on the depth at which their respective rays intersect objects. Pixels in planes which are not in focus are blurred into a new image as circles whose diameter equals the circle of confusion and whose alpha values, which dictate transparency, are inversely proportional to the circle's area. For our experiment, the circle of confusion is calculated to be 913 μm, while the width of the image is 1616 μm.

3 Comparison of Model with Experimental Results

In order to verify our computational model, we designed an experiment and compared the experimental results with the results obtained from the model. Figure 3 shows a schematic of the experimental setup. A xenon lamp was used as white light illumination source and the light intensity was reduced by introducing a 2-cm diameter aperture and neutral density (ND) filters in the beam path. The image of a tree[17] was printed on a transparency slide and placed behind the

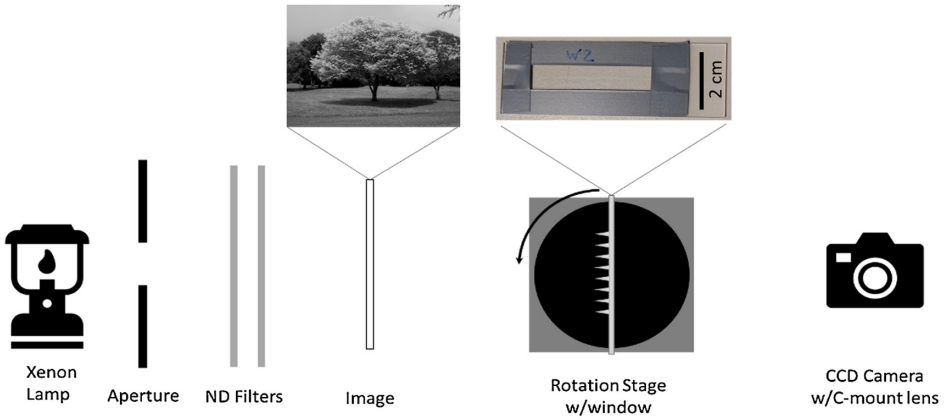

Fig. 3 Schematic of the experimental setup.

ND filters. A window coated with ETCs was mounted on a rotation stage with the ETC tips pointing toward the light source. The window area was 0.8 cm × 3 cm, ETC lines were parallel to the short side and along the rotation axis. This geometry of the window allows for rotation with only minor limitations due to edges. For reference, the experiment was also performed with a window without ETCs. ETC printing has been described elsewhere.[2–4,21,22] Images were taken with a CCD camera. The distance from camera to window was 25 cm, distance from camera to image 125 cm, the focal length of the camera was 75 mm, the aperture diameter of the camera was 3.41 mm, and the width of the image on the CCD chip was 1.61 mm.

The window was rotated up to 60 deg relative to the normal position shown in Fig. 3 which we define as 0 deg and images were captured at every 10 deg step. To account for fluctuations in the light intensity, every configuration was measured five times and an average was created after performing a drift correction. Figure 4 shows the measured images under (a) 0 deg, (b) 20 deg, (c) 40 deg, and (d) 60 deg. It can be seen that image becomes darker when the ETC window is rotated.

Using the same geometry as in the experiment, we also performed a computational study. Figures 4(e)–4(h) show the result of a high-resolution ray tracing computation. It can be seen that black lines appear caused by the ETCs. If the resolution is lowered to reflect the camera's resolution, the results in Figs. 4(i)–4(l) are obtained. The black lines are still pronounced and the overall appearance is different than those of the experiment. For the images in Figs. 4(m)–4(p), depth of field correction was performed according to Sec. 2.3. The pronounced black lines disappear and the images seem to only become darker when the window is rotated.

For a more quantitative comparison, we used the structural similarity (SSIM) index. This algorithm estimates the subjective similarity between two images by mimicking the functionality of the human visual system. The three criteria which are used to judge similarity are luminance, contrast, and structure. Luminance refers to the comparison of overall brightness between the two images and its calculation involves using the mean values from a small area of pixels. Contrast is the difference in the local range of brightness between two images and its calculation involves using the normalized standard deviation between pixels. The final criterion is meant to represent the difference in local structure between the two images, and its calculation involves taking the inner product of local pixels in one image with local pixels in the other. The first two components range from zero to one, and the last ranges from negative one to one— these are combined to form the total structural similarity index, which ranges from negative one to one.[23]

To use this algorithm in our comparison of ETC-coated windows at various angles, we chose, for each set of images, a reference image. The reference image was always (in computations and experiments) an uncoated window which was generated/measured under the same conditions as the ETC window that was evaluated. This was taken to be the ideal image for each set—an SSIM value lower than one would indicate a deviation from the ideal, and therefore a degradation in image similarity. Values for luminance, contrast, structure, and total SSIM for images generated in various ways are plotted in Fig. 5. In Fig. 5(a), it can be seen that the luminance value decreases with increasing angle which was intuitively expected from the decrease of brightness

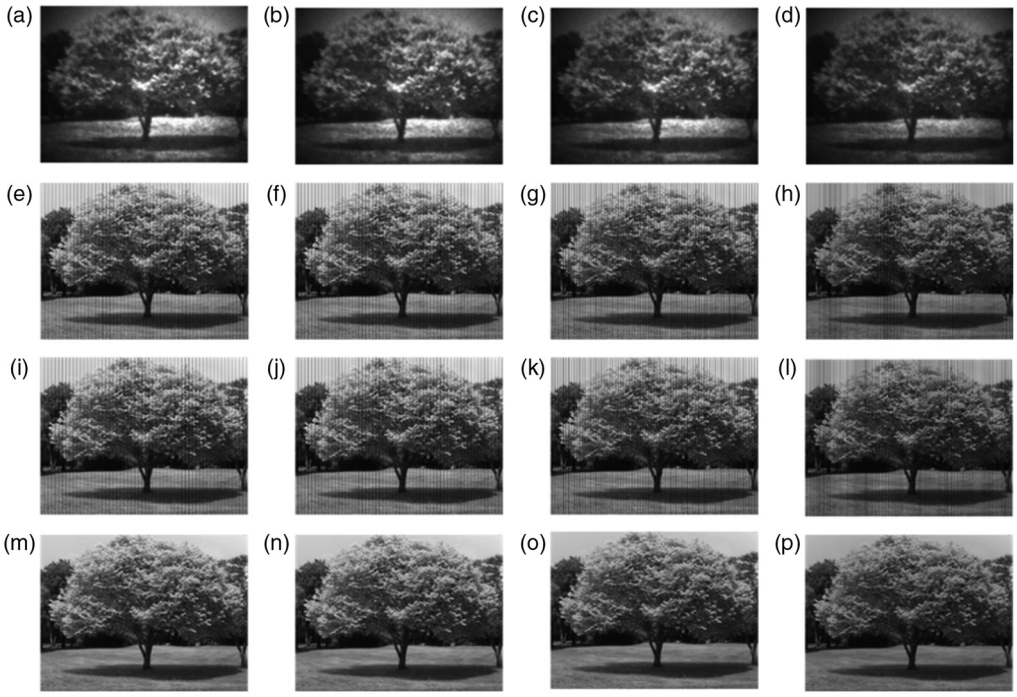

Fig. 4 Series of images seen through ETC windows measured (a–d) and computationally simulated with (e–h) high resolution ray tracing, (i–l) resolution correction, and (m–p) depth of field correction. The images were captured under (a, e, i, m) normal incidence, (b, f, j, n) 20 deg, (c, g, k, o) 40 deg, and (d, h, l, p) 60 deg angle of incidence with rotation axis along the ETC lines.

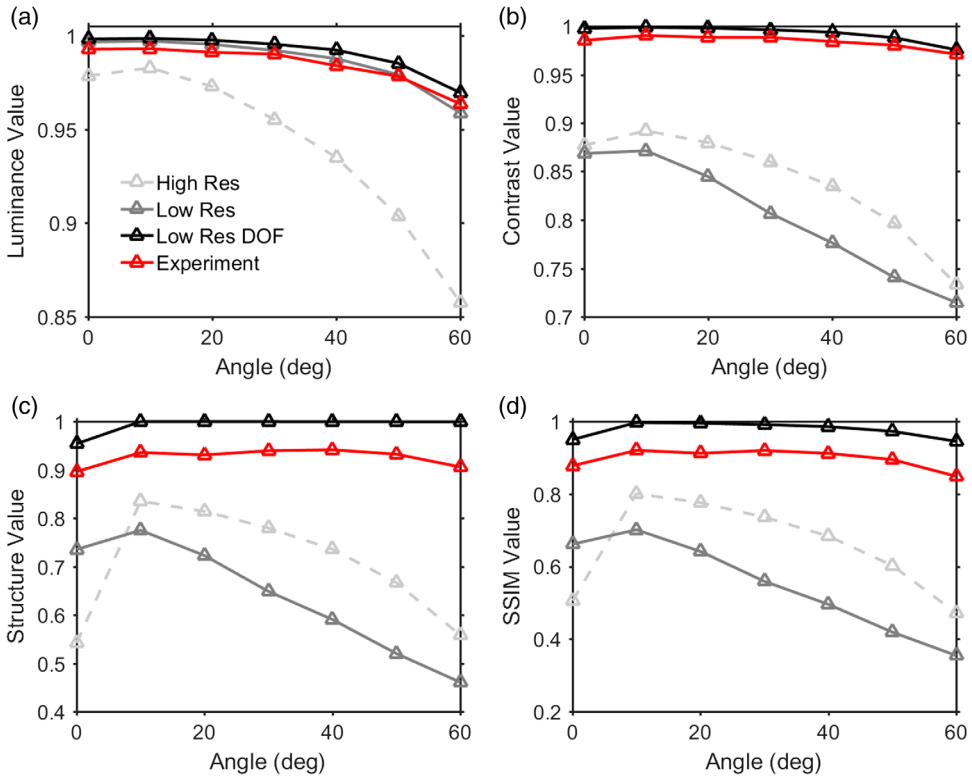

Fig. 5 Quantitative comparison between experimental results and computational simulation. The (a) luminance, (b) contrast, (c) structure, and (d) SSIM values are plotted as a function of the angle of incidence.

easily observable by eye. The low resolution and depth of field corrected simulations match the experimental luminance values well, while high resolution simulations provide a much lower luminance value than observed in the experiments. Figures 5(b) and 5(c) show the contrast and structure value, respectively. Only the depth of field corrected simulation provides results within the experimental tolerance. Without depth of field correction, the image quality degrades too much as can be seen by the black lines in Fig. 4(e)–4(l). This behavior is also observed for the overall SSIM value which is presented in Fig. 5(d). The depth of field corrected structure value is slightly higher than for the measured case which also dominates the SSIM value. This could be due to either fabrication uncertainties or due to the assumption of a slightly too high circle of confusion. Overall, our algorithm using high-resolution ray tracing, with image correction for eye resolution and depth of field, provides reliable results with very good agreement with the experimental results.

To better understand how these experimental CCD camera results relate to a human eye and how variations in length scales affect the appearance of the ETCs, we examine the role of focal length in our model. There are two contributions that the focal length makes to the appearance of objects in the image. The first contribution is the perceived size of the object—that is, what proportion of the total image a particular object takes up. The second contribution affects objects which are not in the focal plane and deals with how much they get blurred.

The first effect is that, for a fixed distance away from an object, the size of the object's image in the image plane is determined by the ratio of the focal distance to the size of the entire image plane. To understand this intuitively, we consider the effect of changing the focal distance or the size of the image plane in Fig. 2. If we increase the size of the image plane but keep the focal length fixed, the spread of rays will be greater. This means that the field of view will be greater, and so any given object will take up a smaller proportion of the field of view. A similar effect is observed when the image plane size remains fixed but the focal distance shrinks. However, if we maintain a constant ratio between the size of the image plane and the focal distance, the spread of rays will remain fixed. Hence, the proportion of the field of view taken up by a given object remains fixed. If we compare these ratios for the eye (17 mm/0.4 mm $\sim$ 42.5) and our CCD camera (75 mm/1.61 mm $\sim$ 47), we see that both are comparable.

The other contribution from the focal length is on the depth of field effects for objects which are outside of the focal plane. This effect is dictated entirely by the circle of confusion on the image plane: a larger circle of confusion corresponds to a blurrier image, while a smaller circle of confusion corresponds to a more sharply focused image. The equation to describe this, derived geometrically in Ref. 12, is: $c = A\frac{|S_2-S_1|}{S_2}\frac{f}{S_1-f}$, where S_1 is the distance from the lens to the focal plane, S_2 is the distance from the lens to the object, A is the aperture size, and f is the focal length. If we assume $f \ll S_1$, the circle of confusion is approximately proportional to the focal length and the aperture size. Furthermore, the appearance will only be affected by the size of the circle of confusion relative to the size of the image plane: a circle of confusion which takes up half the image plane will appear blurrier than one that takes up one quarter of the image plane. When we calculate the ratio between the size of the circle of confusion and the size of the image plane for the camera and the eye, we get $\sim 1/2$ and $\sim 1/4$, respectively. Clearly there is a discrepancy. However, since the contacts in each case are blurred out over such a large portion of the image, the effect in both cases is observed as a dimmed image.

The presented comparison between simulation and experiment shows that our ray optical model accurately describes the experiments for the propagation of incoherent, diffused light. We demonstrated previously that no resonant absorption or (Mie) scattering is present when visible light interacts with triangular silver structures with width >2.5 μm,[14] and that the total transmission intensity can be described with a ray optical formalism. However, close attention needs to be paid to the spatial transmission profile[24] in order to determine the visual appearance. Knowledge on the spatial coherence of the light involved is required to accurately determine the electric field propagation profile behind the window. Our ETC windows consist of periodic structures that could potentially cause Fraunhofer diffraction in the far field, at the location of the observer. For point light sources such as light-emitting diodes, lasers, and any light source observed through an aperture,[25] diffraction patterns are observed. Divitt and Novotny[26] found the spatial coherence of direct sunlight to be 80λ, where λ is the wavelength of the concerned photons. The periodicity of our standard ETC grid is 80 μm and thereby close

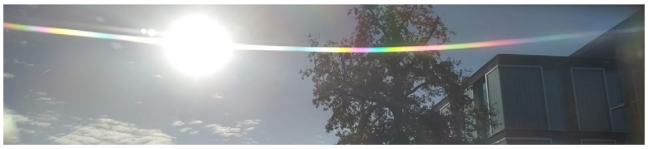

Fig. 6 Picture taken through an ETC window (with ND filters).

to this regime. Sunlight can be viewed as a partially coherent source that can still display restricted diffractive effects. We found that when looking through ETC windows directly at the sun diffraction becomes visible. Figure 6 shows a picture of the sun and our institute building at the University of Twente taken through an ETC window with vertical ETC lines. A rainbow diffraction pattern appears in horizontal direction and perpendicular to the ETC lines. The appearance of the sky, clouds, a tree, and our building are not disturbed by the ETC window as scattered light loses spatial coherence.[27] Hence, for scattered light, which constitutes the majority of the field of view, the assumption of low spatial coherence is valid and a ray optical approach is justified. However, in applications in which undistorted view is crucial, such as in eye glasses and car windshields, and encounter of spatially coherent light sources (e.g., traffic lights) is likely, only the zero-order diffraction peak would be desired.

4 Angle-Dependent Visual Appearance of ETC Windows

Using the above-described model, we investigated the angle-dependent visual appearance of ETC windows. If scenes are observed under an angle the possibility arises for rays redirected by ETCs to fall within the numerical aperture of the eye. Figure 7 shows the rays involved in this process. Figure 7(a) gives a high level overview of all components involved. The observer observes a scene from a dark room through an ETC window under an angle α perpendicular to the window plane. The undisturbed rays are shown in gray and result in an image of sailing boats in water as shown in Fig. 8. Rays that are hitting the bottom of the triangle are coming from the dark room and therefore, darken the picture as described above. Rays that are redirected by the ETCs are shown in red. These rays project an image from a different scene and under a different angle than the undisturbed rays. In the following, we refer to this angle as the β-angle where an angle of 0 deg corresponds to the same scene projected by undisturbed rays. In Fig. 7(b), the area around the window is magnified such that the diffraction of rays at the window becomes apparent. In Fig. 7(c), the scene is further magnified to show the ETCs and their influence on the light redirection.

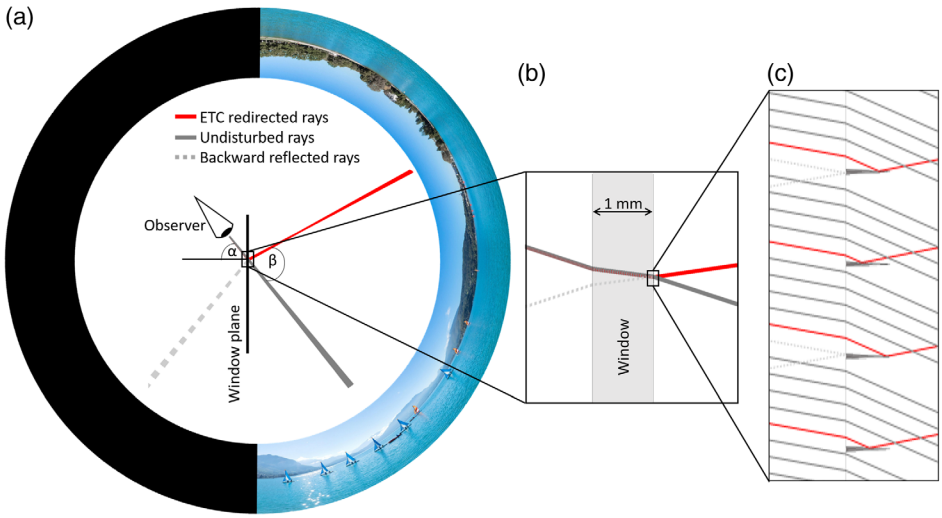

Fig. 7 Visualization of the optical model for scenes observed through an ETC window under an angle.

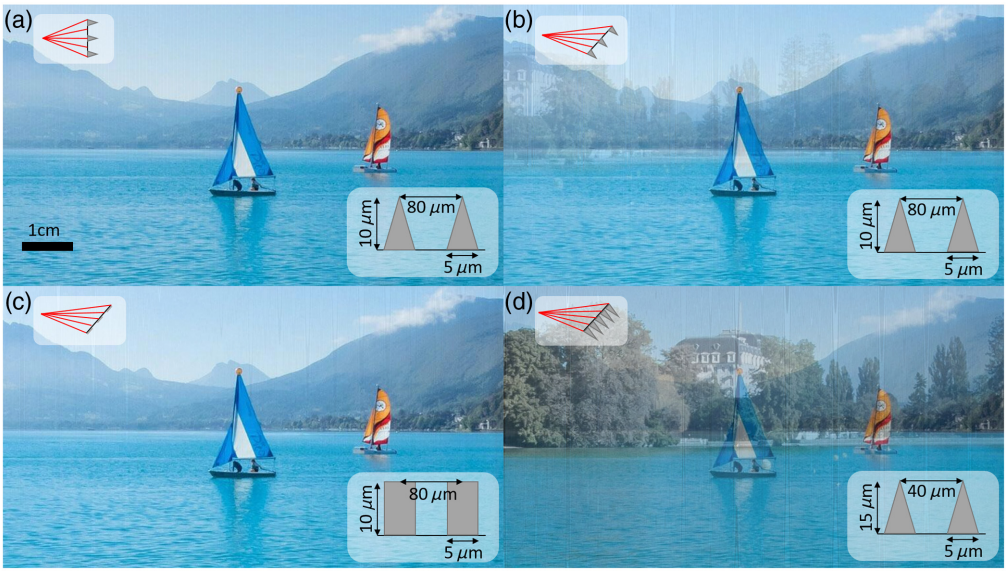

Fig. 8 The same scene observed in four different ways: (a) through an ETC window under normal incidence; (c) through a window with flat contacts under 50 deg viewing angle with a height of 10 and 80 μm periodicity; (b) and (d) through ETC windows under 50 deg viewing angle with ETCs, with (b) 10 μm height and 80 μm periodicity and (d) 15 μm height and 40 μm periodicity.

Figure 8 shows the same scene of sailing boats on a lake observed in four different ways. In Fig. 8(a), the scene is viewed through an ETC window under normal incidence. In Fig. 8(c), the scene is viewed under an angle of 50 deg through a window with flat contacts with 5 μm width and 80 μm periodicity. This image appears undisturbed. In Figs. 8(b) and 8(d), scenes are observed through ETC windows with different periodicity [80 μm (c) and 40 μm (d)] and different ETC height [10 μm (c) and 15 μm (d)]. It can be seen that in both cases a ghost image from a different scene appears. Due to the closer spacing in Fig. 8(d), the ghost image is more pronounced than in Fig. 8(b) and due to the higher aspect ratio in Fig. 8(d) the projected scene is further away from the undisturbed image than in Fig. 8(b). These relations are quantified in Fig. 9. In Fig. 9(a), the percentage of ETC redirected rays that create the ghost image is presented as a function of the viewing angle α. The relation is shown for different periodicities and different aspect ratios. The closer the spacing and the higher the aspect ratio, the higher the percentage of redirected rays. Figure 9(b) shows the β-angle of the ghost image scene. At the onset of the ghost image the β-angle is at 0 deg which corresponds to the undisturbed image. With increasing viewing angle α, the β-angle increases which means that the projected ghost scene moves further and further away from the undisturbed scene. The higher the aspect ratio the earlier the onset and the difference compared to the undisturbed image. In conclusion,

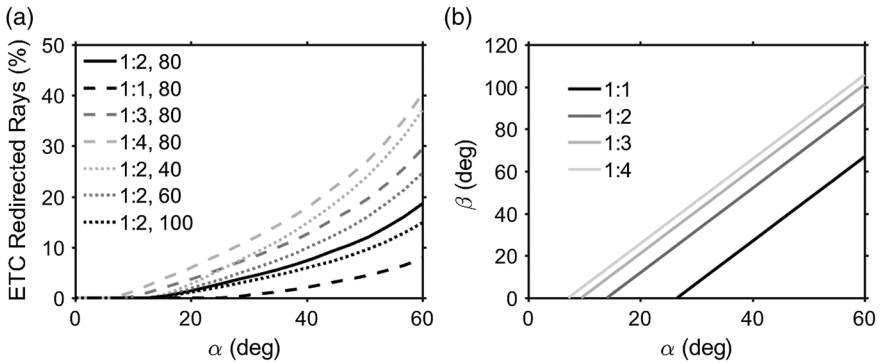

Fig. 9 (a) Percentage of ETC redirected rays as a function of the viewing angle α for different ETC periodicities and different aspect ratios. 1:2, 80 means: aspect ratio 1:2, periodicity 80 μm. (b) β-angle of the redirected rays as a function of the viewing angle α for different aspect ratios.

Fig. 9 shows that the appearance and strength of ghost images strongly depends on the geometry of the ETCs and becomes less pronounced for ETCs with scarce spacing and low aspect ratio. In order to increase the conductivity of ETC superstrates, the aspect ratio needs to be high and the spacing dense. Furthermore, dense spacing also improves light trapping. Therefore, designing optimal ETC superstrates for use in solar windows requires careful design to find the optimal configuration that fulfills all electrical, optical, and appearance requirements.

5 Summary

We have investigated the visual appearance of ETC windows that can be used as transparent, conductive superstrates for solar windows. We developed a ray optical model to computationally determine the visual appearance, taking the properties of human eyes into account. We found that our model provides good description of the experimental results, as long as the spatial coherence of the light is low, such as is the case for scattered sunlight. We quantified this finding using the SSIM. Scenes observed through an ETC window under a perpendicular viewing angle appear undisturbed but slightly darkened by the redirection of light. This result is equivalent to the visual appearance of flat opaque lines with the same dimensions. If scenes are viewed through an ETC window under an angle, ghost images of a different scene are observed. These images result from the rays that are redirected by the ETCs. The magnitude and angle of the observed scene relative to the normal scene depend on the aspect ratio and on the periodicity of the ETCs. For solar windows, these parameters can be optimized along with the geometry dependent conductivity, effective transparency, and light trapping.

Acknowledgments

We thank Pim Venderbosch, Chris van de Stadt, and Cock Harteveld for help with setting up the experiments. We thank Matthijs Velsink for advice regarding the design of the ray tracing program. We thank Pim Venderbosch, Haider Zia, Sisir Yalamanchili (Caltech), and Thomas Russell (ETC Solar), the Caltech ETC team and the COPS chair for helpful discussion. We thank Peter Van den Wyngaert – www.littleplanet.be for photo usage permission. R.S. was funded by the University of Twente tenure-track start-up funding. L.M. acknowledges Lawrence University, Wisconsin, USA, for funding to be awarded as part of the Lawrence University Research Fellow (LU-RF) program.

References

1. M. Morales-Masis et al., "Transparent electrodes for efficient optoelectronics," *Adv. Electron. Mater.* **3**(5), 1600529 (2017).
2. R. Saive et al., "Silicon heterojunction solar cells with effectively transparent front contacts," *Sustain. Energy Fuels* **1**, 593–598 (2017).
3. R. Saive et al., "Effectively transparent front contacts for optoelectronic devices," *Adv. Opt. Mater.* **4**(10), 1470–1474 (2016).
4. R. Saive et al., "Effectively transparent contacts (ETCs) for solar cells," in *IEEE 43rd Photovoltaic Specialists Conf. (PVSC)*, IEEE, pp. 3612–3615 (2016).
5. R. Saive et al., "Enhanced light trapping in thin silicon solar cells using effectively transparent contacts (ETCs)" in *IEEE 44rd Photovoltaic Specialists Conf. (PVSC)*, IEEE (2017).
6. R. Saive, T. C. Russell, and H. A. Atwater, "Enhancing the power output of bifacial solar modules by applying effectively transparent contacts (ETCs) with light trapping," *IEEE J. Photovoltaics* **8**(5), 1183–1189 (2018).
7. K.-S. Chen et al., "Semi-transparent polymer solar cells with 6% PCE, 25% average visible transmittance and a color rendering index close to 100 for power generating window applications," *Energy Environ. Sci.* **5**(11), 9551–9557 (2012).
8. M. G. Kang et al., "Manufacturing method for transparent electric windows using dye-sensitized TiO_2 solar cells," *Solar Energy Mater. Solar Cells* **75**(3–4), 475–479 (2003).
9. A. A. Husain et al., "A review of transparent solar photovoltaic technologies," *Renew. Sustain. Energy Rev.* **94**, 779–791 (2018).

10. G. E. Eperon et al., "Neutral color semitransparent microstructured perovskite solar cells," *ACS Nano* **8**(1), 591–598 (2013).
11. G. T. Koishiyev and J. R. Sites, "Impact of sheet resistance on 2-D modeling of thin-film solar cells," *Solar Energy Mater. Solar Cells* **93**(3), 350–354 (2009).
12. J. Van Deelen et al., "Improvement of transparent conducting materials by metallic grids on transparent conductive oxides," *Thin Solid Films* **555**, 159–162 (2014).
13. R. Saive et al., "Transparent, conductive and lightweight superstrates for perovskite solar cells and modules," in *IEEE 45th Photovoltaic Specialists Conf. (PVSC)*, IEEE (2018).
14. R. Saive and H. A. Atwater, "Mesoscale trumps nanoscale: metallic mesoscale contact morphology for improved light trapping, optical absorption and grid conductance in silicon solar cells," *Opt. Express* **26**(6), A275–A282 (2018).
15. A. V. Goncharov et al., "Reconstruction of the optical system of the human eye with reverse ray-tracing," *Opt. Express* **16**(3), 1692–1703 (2008).
16. J. Arvo, "Backward ray tracing," in *Developments in Ray Tracing, Computer Graphics, Proc. of ACM SIGGRAPH 86 Course Notes*, pp. 259–263 (1986).
17. F. Wilde, "Bright green tree–Waikato," 2005, https://commons.wikimedia.org/wiki/File:Bright_green_tree_-_Waikato.jpg (15 July 2019).
18. P. van den Wyngaert, 360° Imagery, 2018, https://www.littleplanet.be (20 July 2018).
19. J. S. D. M. Yanoff, "Ophthalmology," *Elsevier Health Sciences*, Chapter 2.6., Elsevier/Oxford, New York/Sydney (2009).
20. J. Demers, *GPU Gems: Programming Techniques, Tips and Tricks for Real-Time Graphics*, Addison-Wesley Professional, Chapter 23, Pearson Education, Inc., New Jersey (2004).
21. R. Saive, C. R. Bukowsky, and H. Atwater, "Three-dimensional nanoimprint lithography using two-photon lithography master samples," arXiv:1702.04012v1 (2017).
22. R. Saive et al., "Fabrication processes for effectively transparent contacts," U.S. Patent No. 15/999, 264 (2019).
23. Z. Wang et al., "Image quality assessment: from error visibility to structural similarity," *IEEE Trans. Image Process.* **13**(4), 600–612 (2004).
24. T. Gao et al., "Fundamental performance limits and haze evaluation of metal nanomesh transparent conductors," *Adv. Opt. Mater.* **6**(9), 1700829 (2018).
25. F. L. Pedrotti, L. M. Pedrotti, and L. S. Pedrotti, *Introduction to Optics*, Cambridge University Press, Cambridge (2017).
26. S. Divitt and L. Novotny, "Spatial coherence of sunlight and its implications for light management in photovoltaics," *Optica* **2**(2), 95–103 (2015).
27. P. Sebbah, *Waves and Imaging Through Complex Media*, Springer Science & Business Media, Dordrecht (2001).

Lucas J. Myers is an undergraduate student at Lawrence University in Appleton, Wisconsin, where he plans to receive his BA degree in physics and mathematics in 2019. He has completed research projects in the fields of biophysics and condensed matter. Most recently, he completed a project studying effectively transparent contacts in solar windows at the University of Twente, Netherlands. He plans to pursue his PhD in physics at the University of Minnesota studying condensed matter theory.

Harry A. Atwater is the Howard Hughes professor of applied physics and materials science at the California Institute of Technology. His scientific interests have two themes: light-matter interactions in nanophotonic materials and solar energy conversion. He is an early pioneer in nanophotonics and plasmonics; he gave the name to the field of plasmonics. He is the founding director of the Resnick Sustainability Institute at Caltech and currently director of the DOE Joint Center for Artificial Photosynthesis.

Rebecca Saive is an assistant professor of applied physics/nanophotonics at the University of Twente, Netherlands. Furthermore, she is the CTO of ETC Solar, an award winning California Institute of Technology (Caltech) spin-off commercializing effectively transparent contacts (ETCs). From 2014 to 2018 she was a postdoc and later a senior research scientist at Caltech. She obtained her PhD at the University of Heidelberg, Germany and her master's degree at the Technical University of Munich.